Carrier scattering, mobilities, and electrostatic potential in monolayer, bilayer, and trilayer graphene

Wenjuan Zhu,[*] Vasili Perebeinos, Marcus Freitag, and Phaedon Avouris[†]
IBM Thomas J. Watson Research Center, Yorktown Heights, New York 10598, USA
(Received 5 August 2009; revised manuscript received 20 October 2009; published 2 December 2009)

The carrier density and temperature dependence of the Hall mobility in monolayer, bilayer, and trilayer graphene has been systematically studied. We found that as the carrier density increases, the mobility decreases for monolayer graphene, while it increases for bilayer/trilayer graphene. This can be explained by the different density of states in monolayer and bilayer/trilayer graphenes. In monolayer, the mobility also decreases with increasing temperature primarily due to substrate surface polar phonon scattering. In bilayer/trilayer graphene, on the other hand, the mobility increases with temperature because the electric field of the substrate surface polar phonons is effectively screened by the additional graphene layer(s) and the mobility is dominated by Coulomb scattering. We also find that the temperature dependence of the Hall coefficient in monolayer, bilayer, and trilayer graphene can be explained by the formation of electron and hole puddles in graphene. This model also explains the temperature dependence of the minimum conductance of monolayer, bilayer, and trilayer graphene. The electrostatic potential variations across the different graphene samples are extracted.

I. INTRODUCTION

In the past few decades, the semiconductor industry has grown rapidly by offering every year higher function per cost. The major driving force of this performance increase is device scaling. However, scaling is becoming more and more difficult and costly as it approaches its scientific and technological limits. An alternative path for future development is needed. Some innovations use new computational state variables, such as spins or magnetic flux instead of charges.[1,2] Other approaches adopt new materials such as carbon nanotubes and graphene to replace silicon.[3] In 2004, single atomic layer graphene was first produced by mechanical exfoliation.[4] This enabled researchers to access and to study this promising material.

Graphene is a two-dimensional (2D) material containing carbon atoms tightly bonded together in a honeycomb arrangement.[5] Monolayer graphene has zero band gap and massless linear dispersion $E_F = \hbar v_F k$, with a Fermi velocity $v_F = 10^6$ m/s. Bilayer graphene, on the other hand, has a parabolic band structure with an effective mass $m = 0.037 m_e$,[6] determined by the interlayer coupling. The band gap in bilayer graphene can be varied by means of an external perpendicular electrical field.[7–9] Trilayer graphene has a similar dispersion relation as bilayer graphene with parabolic bands, except that the effective mass is larger $m = 0.052 m_e$.[6] Recently, it was proposed that trilayer graphene is semimetallic with a tunable band overlap.[10]

The key property of interest in graphene for electronic applications is the fast electronic transport expressed by its high carrier mobility. Suspended monolayer graphene has been shown to have extremely high mobilities (up to 200,000 cm²/Vs),[11,12] however, this value is strongly reduced in the supported structure by impurity and phonon scattering.[13–17] Since monolayer graphene has no band gap, it is not directly suitable for digital electronics, but is very promising for analog, high frequency applications[18] and interconnects.[5,19] Transport in bilayer and trilayer graphene

has been studied less extensively. Because of their different band structures and screening properties, the contributions of the various scattering mechanisms are expected to change in these layers and different electronic applications are possible. For example, bilayer graphene could at high electrical fields develop a significant band gap to be employed in digital electronics.[9]

Here, we present a systematic study of the Hall carrier mobilities and their temperature dependence for monolayer, bilayer, and trilayer graphenes in order to determine the importance of the different scattering mechanisms in limiting these mobilities at technologically relevant carrier densities. We also use Hall-effect measurements to determine the electrostatic potential variations in the graphene layers at low carrier densities.

II. EXPERIMENT

The graphene layers were deposited through mechanical exfoliation of graphite on a 300 nm SiO₂ film grown on a silicon substrate. The number of layers deposited was determined by the changes in the reflectance of green light[10,20] and by Raman spectroscopy (see Appendix). The Hall-bar geometry was fabricated using oxygen plasma, while the electrodes were made of Ti/Pd/Au. The Si substrate itself was used as a back gate. The resistivity of the silicon substrate was $10^3 \sim 10^4$ Ohm-cm. The magnetic field was +/−2 T and the samples were measured in high vacuum ($10^{-6} \sim 10^{-8}$ Torr) in the temperature range of 4.2 to 350 K. The carrier density n was extracted from the Hall voltage V_H: $n = -IB/eV_H$, where I is current, B is the magnetic field, and e is the electron charge. The Hall mobility was extracted using the relation: $\mu = \sigma_{xx}/en$, where σ_{xx} is the four-probe conductivity along the current direction. The gate lengths (the distance between two voltage sensing terminals) varied from 2 to 4 μm and the Hall-bar widths were from 0.5 to 4 μm. The temperature dependence of mobility was mea-
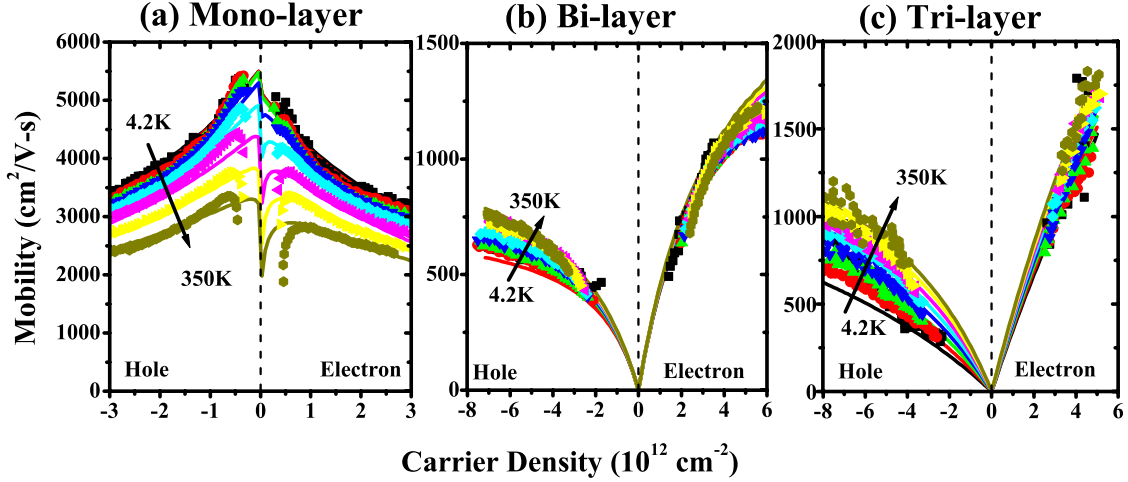
FIG. 1. (Color online) Hall mobility as a function of carrier density at temperatures from 4.2 to 350 K in (a) monolayer graphene, (b) bilayer graphene, and (c) trilayer graphene. The symbols are the measured data, the lines are fits.

sured on two monolayer graphene, three bilayer graphene and two trilayer graphene devices.

III. MOBILITY AND CARRIER SCATTERING

The mobility and scattering mechanism in monolayer graphene has been studied both experimentally[13,21,22,17] and theoretically considering Coulomb scattering,[23,24] short-range scattering,[14] phonon scattering by graphene phonons,[15,25] substrate surface polar phonon scattering,[26] midgap states,[27] and roughness.[16] There are some reports on mobility extracted from two terminal measurements on bilayer[28] and trilayer graphene.[10] However, the temperature dependence of Hall mobility and the scattering mechanisms for bilayer and trilayer graphene has not been established yet. In this section, we will discuss the temperature dependence of Hall mobility for bilayer and trilayer graphene and compare it with monolayer graphene.

Figure 1 shows the carrier density dependence of the mobility at various temperatures (from 4.2 to 350 K) for monolayer, bilayer, and trilayer graphene, respectively. We see that, as the carrier density increases, the mobility decreases for monolayer graphene, while it increases for bilayer and trilayer graphene.

The temperature dependence of the hole mobility at various carrier densities for these layers is shown in Fig. 2. We observe that the mobility decreases with temperature for monolayer graphene, especially when the temperature is above ~200 K, while it increases with temperature for bilayer and trilayer graphenes.

These different trends in the variation in the carrier mobility in monolayer and bilayer/trilayer graphenes can be understood by differences in their density-of-states and the additional screening of the electrical field of substrate surface polar phonons in bilayer/trilayer graphenes. A detailed analysis is given below.
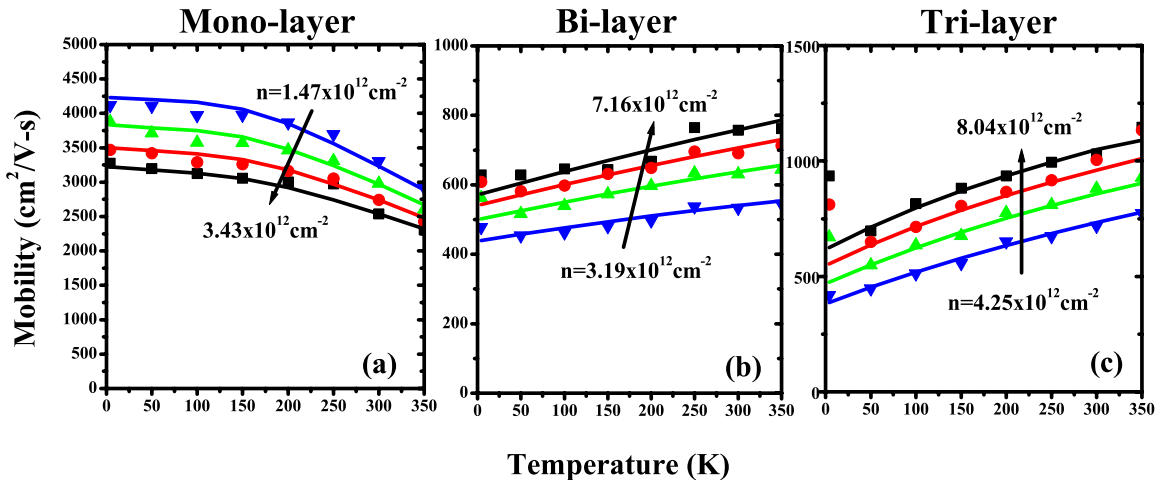

FIG. 2. (Color online) Hall mobility for holes as a function of temperature at various carrier densities in (a) monolayer graphene, (b) bilayer graphene, and (c) trilayer graphene. The symbols are the measured data, the lines are fits.

A. Carrier density dependence of the mobility at low temperatures

At low temperatures, the dominant scattering mechanism is Coulomb scattering by impurities and short-range scattering by defects. The overall mobility can be found using a Matthiessen's rule $\mu_{total}^{-1} \approx \mu_C^{-1} + \mu_{sr}^{-1}$.[14] The transport scattering rate can be calculated using the Fermi-Golden rule[14]

$$\frac{1}{\tau(E_k)} = \frac{2\pi n_i}{\hbar} \int_{k'} \frac{d^2 k'}{(2\pi)^2} \left| \frac{V(q)}{\varepsilon(q)} \right|^2$$
$$\times (1 + \cos\theta_{kk'})(1 - \cos\theta_{kk'})\delta(E_k - E_{k'}), \quad (1)$$

where n_i is the concentration of the impurity center, $q = |k - k'| = 2k \sin(\theta_{kk'}/2)$, and $\theta_{kk'}$ is the angle between the scattering *in* and *out* wave vectors k and k', $V(q)$ is the matrix element of the scattering potential, $\varepsilon(q)$ is the 2D finite temperature static random-phase-approximation (RPA) dielectric (screening) function appropriate for graphene. Note that the $[1 - \cos(\theta_{kk'})]$ term in Eq. (1) describes contributions from the large angle scattering, while the $[1 + \cos(\theta_{kk'})]$ is due to the matrix element angle dependence. We are interested primarily in the scattering around the Fermi energy E_F. The matrix element is given by $V(q) = \frac{2\pi e^2}{\kappa q}$ for Coulomb scattering, if we assume the scattering charge centers are at the SiO_2-graphene interface, while it is constant for short-range scattering.[14] The energy average scattering time can be written as[14]

$$\langle \tau \rangle = \int dE_k E_k \tau(E_k) \left(-\frac{\partial f}{\partial E_k} \right) \Big/ \int dE_k E_k \left(-\frac{\partial f}{\partial E_k} \right). \quad (2)$$

At low temperatures, the scattering time averaged over energy becomes: $\langle \tau \rangle \approx \tau(E_F)$. The RPA dielectric screening modifies the bare Coulomb interaction $V(q)$ in a monolayer to $\frac{V(q)}{\varepsilon(q)} = \frac{2\pi e^2}{\kappa(q + q_T)}$,[12,23] where κ is a dielectric constant of the environment and $q_T = k_F(4e^2/\kappa\hbar v_F)$, k_F is a Fermi wave vector. Since both bare and screened Coulomb potentials are inversely proportional to k_F, we can describe the scaling of the scattering rate with carrier density n using the bare potential $1/\tau \propto |V(k_F)|^2 D(E_F)$.

The density-of-states $D(E_F)$ in monolayer graphene is proportional to E_F[24]

$$D(E_F) = \frac{2E_F}{\pi(\hbar v_F)^2}, \quad (3)$$

while in bilayer or trilayer graphene it is constant[24]

$$D(E_F) = \frac{2m}{\pi\hbar^2} \quad (4)$$

Here, the Fermi energy $E_F = \hbar v_F k = \hbar v_F \sqrt{\pi n}$ for monolayer,[14] while $E_F = \hbar^2 k^2/2m = \hbar^2 \pi n/2m$ for bilayer or trilayer graphene. Note that in the Boltzmann treatment the mobility is related to the scattering time as $\mu = \frac{eD(E_F)v_F^2\langle\tau\rangle}{2n}$, which reduces to $\mu_{Mono} = \frac{ev_F^2\langle\tau\rangle}{E_F}$ in a monolayer and to $\mu_{Multi} = \frac{e\langle\tau\rangle}{m}$ in bilayer and trilayer graphene. Our devices have a few μm channel lengths, which justifies using a diffusive transport mechanism to analyze our data. We can estimate the mean free path in both monolayers and multilayers using $\lambda = \hbar\mu\sqrt{\pi n}/e$ and the mobility values from Fig. 1 at a characteristic carrier density of $n = 3 \times 10^{12}$ cm^{-2}. We obtain: $\lambda \approx 70$ nm in the monolayer, $\lambda \approx 10$ nm in bilayer and trilayer.

For monolayer graphene, the mobility limited by Coulomb scattering was found to be independent of carrier density, $\mu_{C\_Mono} \propto$ constant, and the mobility limited by short-range scattering was found to be inversely proportional to the carrier density for monolayer, $\mu_{sr\_Mono} \propto 1/n$.[14]

For bilayer and trilayer graphene, based on Eqs. (1), (2), and (4), we find that the mobility limited by Coulomb scattering is proportional to the carrier density, $\mu_{C\_Multi} \propto n$, while the mobility limited by short-range scattering is constant: $\mu_{sr\_Multi} \propto$ constant. These considerations explain qualitatively why the mobility at 4.2K for monolayer graphene decreases with increasing carrier density, while it increases with increasing carrier density for bilayer and trilayer graphene, as shown in Figs. 1(a)–1(c).

B. Temperature dependence of mobility

The mobility in monolayer graphene decreases rapidly with increasing temperature when the temperature is above about 200 K (see Fig. 2(a)). This is primarily due to scattering by thermally excited surface polar phonons of the SiO_2 substrate.[13,26,29] The SiO_2 optical phonons at the substrate/graphene interface modulate the polarizability, which produces an electric field that couples to the carriers in graphene. The coupling or the field depends exponentially on the substrate graphene distance. At the Van der Waals distance of about 0.35 nm, it is much stronger than the coupling of the carriers to the acoustic phonons of graphene. There are two important surface phonons in SiO_2 with energies of about 59 and 155 meV (Refs. 26 and 30) and the coupling is determined by the dielectric polarization field: $\vec{P} \propto \sqrt{\hbar\omega_{so}(\frac{1}{\varepsilon_\infty + 1} - \frac{1}{\varepsilon_0 + 1})}$, where ω_{so} is a surface polar phonon frequency, ε_0 and ε_∞ are the low- and high-frequency dielectric constants of SiO_2 correspondingly, and the dielectric constant of air is one. The substrate surface polar phonon scattering is proportional to the phonon population number such that the scattering rate can be expressed as: $\tau_{ox}^{-1} \propto \sum_i \frac{c_i}{e^{\hbar\omega_i/\kappa_B T} - 1}$, where $\hbar\omega_i$ is the phonon energy. For SiO_2, there are two dominant surface phonon modes at $\hbar\omega_1 = 59$ meV and $\hbar\omega_2 = 155$ meV with the ratio of $c_2/c_1 \approx 6.5$, which is determined by the dielectric constants in SiO_2.[26] Thus, as the temperature is increased, the mobility is expected to decrease drastically. For bilayer and trilayer graphene, however, the mobility increases instead of decreasing as the temperature increases. This is due to the fact that Coulomb scattering is dominant for these bilayer and trilayer graphene devices and the substrate surface polar phonon induced field is to some extent screened by the additional graphene layer(s).[31,32]

In bilayer and trilayer graphene samples, the temperature dependence of mobility is mainly determined by Coulomb scattering. Due to the parabolic band structure, the energy averaging of the Coulomb scattering time can result in the mobility increasing proportionally to temperature: $\mu \propto k_B T$.[33] The dielectric screening, which we ignored in the above
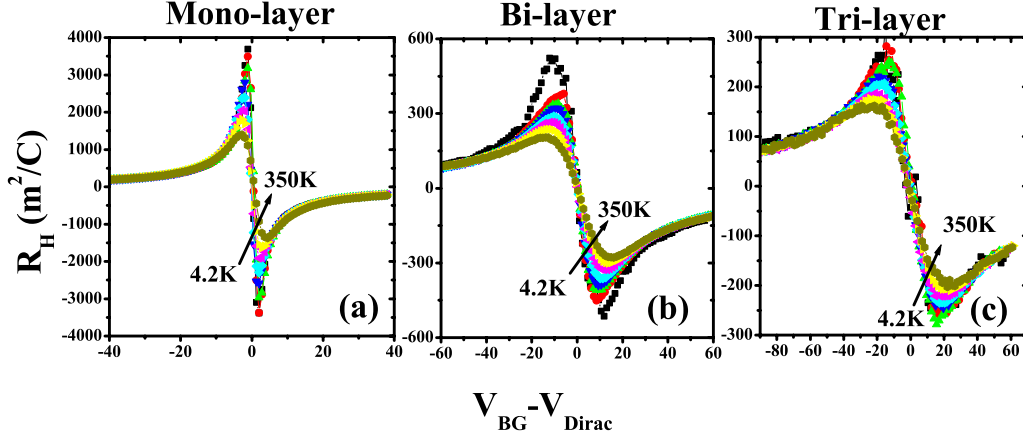
FIG. 3. (Color online) Hall coefficient as a function of V_{BG}-V_{Dirac} in (a) monolayer graphene, (b) bilayer graphene, and (c) trilayer graphene.

analysis, could also introduce an additional temperature dependence. For monolayer, however, it was found that the temperature dependence of Coulomb scattering is very weak, when $k_B T \ll E_F$,[23] which is the temperature and carrier density range we are investigating here.

The temperature dependence of the mobility limited by short-range scattering is independent of temperature for bilayer and trilayer graphene, since the density-of-states, the matrix element and the screening function are all energy independent. In monolayer graphene, the temperature dependence of conductivity or mobility that is limited by short-range scattering is nearly constant, when $k_B T \ll E_F$.[24] On the other hand, the mobility limited by the graphene acoustic phonons in monolayer graphene is inversely proportional to temperature.[34] However, since the magnitude of the mobility limited by graphene phonon scattering is of the order of 10^5 cm^2/V-s,[15,12] i.e., much larger than the mobilities limited by the Coulomb and short-range scattering mechanisms discussed above, we neglect it in multi-layer graphenes.

Based on the above discussion, we fit the measured carrier mobilities using the following model for monolayer and bilayer or trilayer graphene.

For monolayer graphene, at 4.2 K, the mobility can be expressed as: $\mu_{4.2K\_Mono}^{-1} \approx \mu_{C\_Mono}^{-1} + \mu_{sr\_Mono}^{-1}$, where $\mu_{C\_Mono} = S_C$ and $\mu_{sr\_Mono} = \frac{S_{sr}}{n}$ with S_C, S_{sr}, as fitting parameters determined by the Coulomb and short-range scattering, respectively. At high temperatures, the mobility can be expressed as

$$\mu_{Mono}^{-1} \approx \mu_{4.2K\_Mono}^{-1} + \mu_{gr\_Mono}^{-1} + \mu_{ox\_Mono}^{-1}, \quad (5)$$

where $\mu_{gr\_Mono} = \frac{S_{gr}}{n*T}$ and $\mu_{ox\_Mono} = S_{ox} n^\alpha (\frac{1}{e^{(59 \ meV)/\kappa_B T} - 1} + \frac{6.5}{e^{(155 \ meV)/\kappa_B T} - 1})^{-1}$ with S_{gr}, S_{ox}, and α as fitting parameters determined by the graphene acoustic phonon and substrate surface polar phonon scattering, respectively.

For bilayer and trilayer graphene, the mobility can be expressed as

$$\mu_{Multi}^{-1} \approx \mu_{C\_Multi}^{-1} + \mu_{sr\_Multi}^{-1}, \quad (6)$$

where we find $\mu_{C\_Multi} = (A + B \cdot T) \cdot n$, $\mu_{sr\_Multi} = C$ and A, B, and C are fitting parameters.

The fitting results for monolayer, bilayer, and trilayer graphenes are shown in Figs. 1(a)–1(c) and 2(a)–2(c). The symbols are the measured data and the lines are the fits. We see that these formulas fit the measured data very well.

One important point is that the mobility limited by Coulomb and short-range scattering for bilayer/trilayers is inversely proportional to the square of the effective mass. This means the more graphene layers, the heavier the effective mass, leading to a higher degradation of the mobility limited by Coulomb and short-range scattering for the same impurity concentration. This is currently a disadvantage for multilayer graphenes. However, when the impurity concentration of the samples and the substrate are significantly reduced by process optimization and since the surface polar phonon scattering in bilayer or trilayer graphene is significantly reduced by screening, the mobility in bilayer and trilayer graphenes can be significantly higher than the mobility in monolayer graphene at room temperature in unsuspended devices. Note that graphite has the highest mobility reported so far,[35] although it cannot be switched off. In addition, electrical noise, which is very important in electronic applications, is significantly reduced in bilayer and trilayers.[36]

IV. HALL COEFFICIENT

Besides the Hall mobility, another important aspect of the current transport is the carrier density n, which is determined by the electronic structure and can be extracted from the Hall coefficient R_H ($n = \frac{-1}{e R_H}$, when only one type of carrier is dominant). The Hall coefficient is defined as $R_H = V_H / I_H B$, where V_H is the measured Hall voltage, I_H is the constant source current and B is the applied magnetic field. To investigate the temperature dependence of carrier density, the temperature dependence of Hall coefficient is analyzed. Figures 3(a)–3(c) shows the Hall coefficient as a function of the back-gate voltage, V_{BG}-V_{Dirac}, at various temperatures (from 4.2 to 350 K) for monolayer, bilayer, and trilayer graphene, respectively. As the temperature is increased, the height of the peak is reduced (or the slope of $|R_H|$ vs V_{BG} decreases) for all graphene layers. This could be explained by either band overlap or by the formation of electron and hole

puddles in graphene near the Dirac point. However, no band overlap is expected in monolayer and in bilayer graphene, therefore we suggest that puddle formation is the dominant mechanism for the observed temperature dependence. The electron and hole puddles were previously observed in scanning tunneling spectroscopy measurements.[37,38] The existence of electron and hole puddles was attributed to the intrinsic ripples[5,39,40] in graphene and extrinsic charge-induced inhomogeneites in the carrier density.[37,41]

The ambipolar Hall coefficient is given by[42]

$$R_H = \frac{n_h \mu_h^2 - n_e \mu_e^2}{e(n_h \mu_h + n_e \mu_e)^2}, \qquad (7)$$

where n_h and μ_h (n_e and μ_e) are hole (electron) carrier density and mobility. The gate voltage is related to the carrier density by the following equation:[43]

$$V_{BG}\text{-}V_{Dirac} = e(n_e - n_h)\left(\frac{1}{C_{ox}} + \frac{1}{C_q}\right), \qquad (8)$$

where C_{ox} is the oxide capacitance and C_q is the quantum capacitance. For monolayer graphene, the quantum capacitance is $C_q = \frac{2Ee^2}{\pi \hbar^2 v_F^2}$. For bilayer and trilayer graphene, $C_q = \frac{2me^2}{\pi \hbar^2}$. For a 300 nm SiO$_2$, the quantum capacitance $C_q \gg C_{ox}$ when carrier density is larger than 2×10^{11} cm^{-2} for monolayer graphene and $C_q \gg C_{ox}$ at any carrier density for bilayer and trilayer. Therefore, Eq. (8) can be reduced to $e(n_e - n_h) = C_{ox}(V_{BG}\text{-}V_{Dirac})$. For large gate voltages, when only one type of carriers is present, Eq. (7) reduces to $R_H = \frac{-1}{C_{ox}(V_{BG}\text{-}V_{Dirac})}$, which is used to determine the gate oxide capacitance for the electron and hole branches. In the vicinity of the Dirac (midgap) point, which we define as the point where $R_H = 0$, we assume that the hole and electron carrier density are equal to each other, i.e., $n_e = n_h = n_{Dirac}/2$, where n_{Dirac} is the total carrier density at the Dirac point.

For monolayer graphene, at low carrier density, we can assume $\mu_{e\_Mono} = \mu_{h\_Mono}$ near Dirac point, since the dominant scattering is Coulomb scattering μ_{c_Mono}, which is independent of carrier density and the measured electron and hole mobilities are roughly equal to those at high carrier density. Then Eq. (7) reduces to

$$R_H \approx \frac{C_{ox}(V_{BG}\text{-}V_{Dirac})}{e^2 n_{Dirac}^2}. \qquad (9)$$

For bilayer and trilayer graphene, the mobility limited by Coulomb scattering is proportional to carrier density ($\mu_{c\_Multi} \propto n$) and the total mobility $\mu_{Multi} \approx \mu_{c\_Multi}$, therefore Eq. (7) is reduced to

$$R_H \approx \frac{3C_{ox}(V_{BG}\text{-}V_{Dirac})}{e^2 n_{Dirac}^2}. \qquad (10)$$

If we assume that the area of the hole and electron puddles is equal in size and simplify the spatial electrostatic potential to a step function with the characteristic peak to peak height of $\pm \Delta$, as illustrated in Fig. 4, then the total carrier density at the Dirac point is
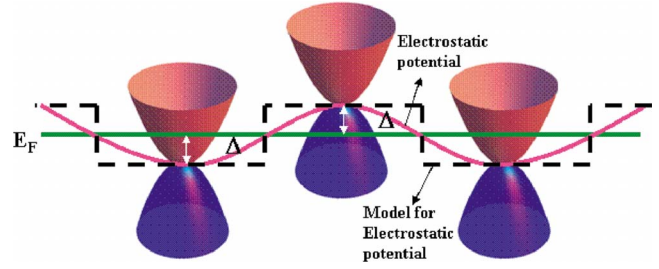

FIG. 4. (Color online) Illustration of the spatial inhomogeneity of the electrostatic potential and the model used in the analysis of the potential variation for monolayer, bilayer, and trilayer graphene.

$$n_{Dirac} = 2n_e = 2n_h$$

$$= \int_{-\Delta}^{\infty} D(E + \Delta)\frac{1}{e^{E/k_B T} + 1}dE$$

$$+ \int_{\Delta}^{\infty} D(E - \Delta)\frac{1}{e^{E/k_B T} + 1}dE. \qquad (11)$$

For monolayer graphene, in the limit $\Delta/kT \gg 1$ Eq. (11) can be simplified as

$$n_{Dirac} \approx \frac{2}{\pi \hbar^2 v_F^2}\left(\frac{\Delta^2}{2} + \frac{\pi^2}{6}k_B^2 T^2\right). \qquad (12)$$

For bilayer and trilayer, from Eqs. (4) and (11), we obtain

$$n_{Dirac} = \frac{2m}{\pi \hbar^2}k_B T\{\ln[1 + \exp(\Delta/k_B T)] + \ln[1 + \exp(-\Delta/k_B T)]\}. \qquad (13)$$

We can extract the electrostatic potential Δ using Eqs. (9) and (12) for monolayer graphene and Eqs. (10) and (13) for bilayer and trilayer graphene. Figure 5 shows the fitting for
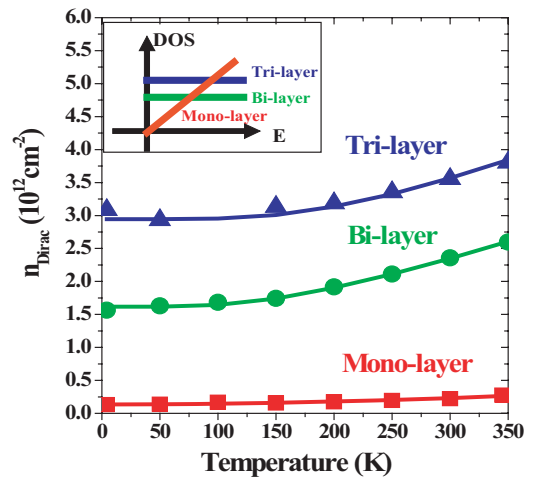

FIG. 5. (Color online) Carrier density at the Dirac point extracted from the Hall coefficient as a function of temperature in monolayer, bilayer, and trilayer graphene. The symbols are the measured data, the lines are fits using Eq. (12) for monolayer graphene and Eq. (13) for bilayer and trilayer graphene. The inset illustrates the density-of-states for monolayer, bilayer, and trilayer graphene.
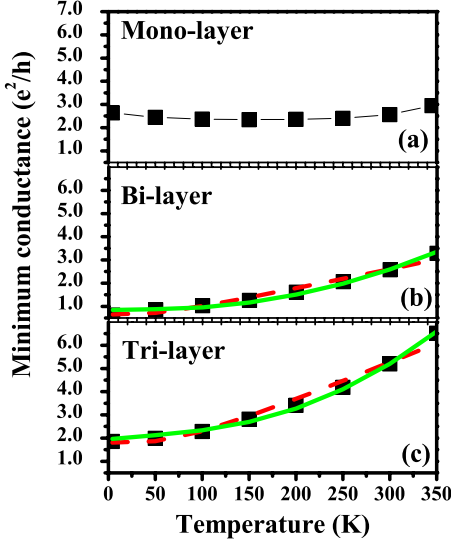
FIG. 6. (Color online) Minimum conductance as a function of temperature for (a) monolayer, (b) bilayer, and (c) trilayer graphene. The symbols are the measured data. In (b) and (c), the red dashed lines are fits that consider only the temperature dependence of the carrier density $n_{Dirac}(T)$ using Eq. (13), while the green solid lines are fits taking into account the temperature dependence of both carrier density and mobility $n_{Dirac}(T)\mu(T)$ using Eq. (14).

monolayer, bilayer, and trilayer graphene. From the fitting, we get $v_F = 1.3 \times 10^6$ m/s and $\Delta = 54$ meV for monolayer graphene, $m = 0.063 m_e$, $\Delta = 31$ meV for bilayer grapheme, and $m = 0.082 m_e$ and $\Delta = 43$ meV for trilayer graphene. These results are consistent with the scanning tunneling spectroscopy measurements on monolayer graphene,[37] which reported a maximum variation in the Dirac point by $\Delta_{max} = 77$ meV.

Note that another possible cause of the temperature dependence of the Hall coefficient is band-overlap. It was proposed that the trilayer graphene is a semimetal with band overlap based on the R_H vs V_{BG} results and the temperature dependence of minimum conductance.[10] However, if we use the band-overlap model, we will obtain a band-overlap larger than 40 meV in all three cases: monolayer, bilayer, and trilayer graphene. Note that we only applied a back-gate voltage and the data region used for fitting is the region near the Dirac point (in between two R_H peaks, i.e., the mixed carrier region only). Therefore, the perpendicular electric field is nearly zero. At this field, both monolayer and bilayer graphenes are known to be zero band-gap materials.[9] Therefore, it is very unlikely that this temperature dependence of the Hall coefficient is due to band overlap. We think this temperature dependence of the Hall coefficient near the Dirac point is most likely due to the electron-hole puddles formation. This finding casts doubt on the proposed value of the band overlap in trilayer graphene.[9] It is clear that local probes like scanning tunneling spectroscopy are needed to resolve this issue.

It should also be mentioned that the carrier density at the Dirac point n_{Dirac} increases with increasing number of layers at a given temperature, as revealed in Fig. 5. This is because the density-of-states near the Dirac point increases with increasing number of layers, as illustrated in the inset of Fig. 5. Since the "on" state carrier density $n_{on} \approx (V_{BG} - V_{Dirac}) C_{ox}/e$ is independent of the number of graphene layers, the carrier density on/off ratio (n_{on}/n_{Dirac}) will decrease with the number of graphene layers. This is one important factor along with screening driving the reduction in the current on/off ratio ($\frac{I_{on}}{I_{off}} = \frac{n_{on}}{n_{Dirac}} \frac{\mu_{on}}{\mu_{Dirac}}$) as the number of layers of graphene increases, and restricts the upper limit of the maximum number of graphene layers to be used for a given on/off ratio requirement.

V. MINIMUM CONDUCTANCE

Based on the temperature dependence of mobility and carrier density discussed in the previous two sections, now we can use these models to explain the temperature dependence of minimum conductance.

The minimum conductances as a function of temperature for monolayer, bilayer, and trilayer graphene are shown in
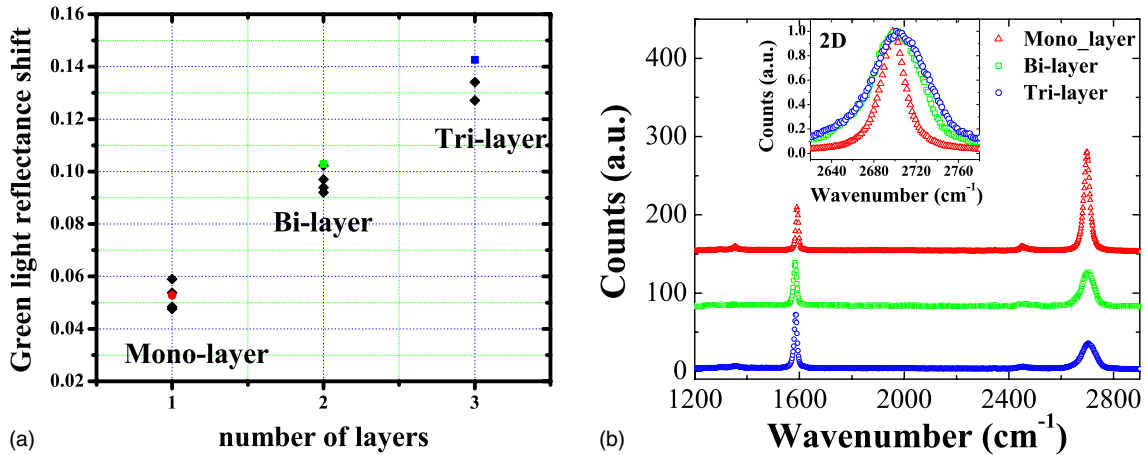

FIG. 7. (Color online) (a) Green light reflectance shift, (b) Raman spectrum of monolayer, bilayer, and trilayer graphenes. The red, green and blue dots in (a) are the flakes measured with Raman as shown in (b). The Raman spectra are offset for clarity. The inset in (b) shows the zoomed-in spectrum of the 2D band, scaled to the maximum intensity value.

the Fig. 6. As the temperature increases, the minimum conductance increases dramatically for bilayer and trilayer graphene, while it is nearly unchanged for monolayer graphene. This can be explained by the temperature dependence of the carrier density and mobility.

For bilayer and trilayer graphene, both the carrier density and the mobility increase with temperature, as shown in Eqs. (13) and (6). Assuming that $\mu_e = n_e(A_e + B_e \cdot T)$ and $\mu_h = n_h(A_h + B_h \cdot T)$, the conductance can be written in the form

$$\sigma(T) = PT^2[\ln(1 + e^{\Delta/(k_B T)}) + \ln(1 + e^{-\Delta/(k_B T)})]^2(1 + rT) \tag{14}$$

where Δ and P are fitting parameters. The parameter r is given by $r = (B_e + B_h)/(A_e + A_h)$, where A and B were extracted previously from the Hall mobility fitting, assuming the temperature dependence of mobility at the Dirac point is similar to the one at higher carrier density. The insets in Figs. 6(b) and 6(c) show the measured minimum conductance as a function of temperature and the fitting results. The red dashed lines are fits considering the temperature of carrier density only, while the green solid lines are fits considering the temperature dependence of both carrier density and mobility. As we can see, the fitting is better when we consider the temperature dependence of both carrier density and mobility. From these fits (including the density dependence of mobility) we obtain $\Delta = 26$ meV and $m = 0.045 m_e$ for bilayer and $\Delta = 36$ meV and $m = 0.066 m_e$ for trilayer graphene. These results are consistent with the results extracted above from the R_H fitting.

VI. SUMMARY

We have performed systematic studies of the transport properties and carrier scattering mechanisms in monolayer, bilayer, and trilayer graphenes as a function of carrier density and temperature using Hall-effect measurements. We found that as the carrier density increases, the mobility decreases for monolayer graphene, while it increases for bilayer and trilayer graphene. This can be ascribed to the different density-of-states for monolayer and bilayer/trilayer graphenes. As the temperature increases, we find that the mobility decreases for monolayer graphene due to the substrate surface polar phonon scattering as in Ref. 11, while it

increases almost linearly with temperature [see Eq. (6)] for bilayer/trilayer graphene. This is attributed to the fact that Coulomb scattering decreases with temperature for bilayer/trilayer graphene due to their parabolic band structure and screening. Furthermore, scattering by the SiO$_2$ substrate surface polar phonons is significantly screened in bilayer/trilayer graphene. We also found that the temperature dependence of the Hall coefficient in monolayer, bilayer, and trilayer graphene can be explained by the formation of electron and hole puddles in the graphene. This model also explains the temperature dependence of the minimum conductance of monolayer, bilayer, and trilayer graphene. The variation in the electrostatic potential along the surface and the effective masses for bilayer and trilayer graphenes are extracted from these measurements.

APPENDIX: OPTICAL CHARACTERIZATION OF GRAPHENE LAYERS

The number of layers in the graphene samples was determined by green light reflectance shifts and Raman spectra. The green light reflectance shift method is based on the optical contrast between graphene and the SiO$_2$ substrate. This has been demonstrated to be an efficient and reliable method to determine the number of graphene layers.[20,10] The green light reflectance shift is defined as: $GRS = (G_s - G_f)/G_s$, where G_f is the green-channel component of the red, green and blue (RGB) value on the flake and G_s is the corresponding value on the substrate. Figure 7(a) shows the green light reflectance shift for monolayer, bilayer, and trilayer graphene. The average shifts for monolayer, bilayer, and trilayer graphene are $GRS_{MG} = 0.053$, $GRS_{BG} = 0.097$, $GRS_{TG} = 0.134$, respectively. The red, green, and blue dots are the flakes measured by Raman scattering as well. The Raman spectrum is shown in Fig. 7(b). While it is difficult to differentiate between bilayer and trilayer graphene from Raman spectra alone, the monolayer graphene stands out with a large 2D to G ratio in agreement with the green light shift method.[44]

*wenjuan@us.ibm.com

†avouris@us.ibm.com

[1] S. A. Wolf, D. D. Awschalom, R. A. Buhrman, J. M. Daughton, S. von Molnár, M. L. Roukes, A. Y. Chtchelkanova, and D. M. Treger, Science **294**, 1488 (2001).

[2] D. A. Allwood, G. Xiong, C. C. Faulkner, D. Atkinson, D. Petit, and R. P. Cowburn, Science **309**, 1688 (2005).

[3] Ph. Avouris, Z. Chen, and V. Perebeinos, Nat. Nanotechnol. **2**, 605 (2007).

[4] K. S. Novoselov, A. K. Geim, S. V. Morozov, D. Jiang, Y. Zhang, S. V. Dubonos, I. V. Grigorieva, and A. A. Firsov, Science **306**, 666 (2004).

[5] A. K. Geim and K. S. Novoselov, Nature Mater. **6**, 183 (2007).

[6] M. Koshino and T. Ando, Phys. Rev. B **76**, 085425 (2007).

[7] E. V. Castro, K. S. Novoselov, S. V. Morozov, N. M. R. Peres, J. M. B. Lopes dos Santos, J. Nilsson, F. Guinea, A. K. Geim, and A. H. Castro Neto, Phys. Rev. Lett. **99**, 216802 (2007).

[8] T. Ohta, A. Bostwick, T. Seyller, K. Horn, and E. Rotenberg, Science **313**, 951 (2006).

[9] Y. Zhang, Tsung-Ta Tang, Caglar Girit, Zhao Hao, Michael C. Martin, Alex Zettl, Michael F. Crommie, Y. Ron Shen, and Feng Wang, Nature (London) **459**, 820 (2009).

[10] M. F. Craciun, S. Russo, M. Yamamoto, J. B. Oostinga, A. F. Morpurgo, and S. Tarucha, Nat. Nanotechnol. **4**, 383 (2009).

[11] K. I. Bolotin, K. J. Sikes, Z. Jiang, D. M. Klima, G. Fudenberg, J. Hone, P. Kim, and H. L. Stormer, Solid State Commun. **146**, 351 (2008).

[12] X. Du, I. Skachko, A. Barker, and E. Y. Andrei, Nat. Nanotechnol. **3**, 491 (2008).

[13] J. Chen, C. Jang, S. Xiao, M. Ishigami, and M. S. Fuhrer, Nat. Nanotechnol. **3**, 206 (2008).

[14] E. H. Hwang, S. Adam, and S. Das Sarma, Phys. Rev. Lett. **98**, 186806 (2007).

[15] E. H. Hwang and S. Das Sarma, Phys. Rev. B **77**, 115449 (2008).

[16] V. V. Cheianov and V. I. Fal'ko, Phys. Rev. Lett. **97**, 226801 (2006).

[17] J. H. Chen, C. Jang, S. Adam, M. S. Fuhrer, E. D. Williams, and M. Ishigami, Nat. Phys. **4**, 377 (2008).

[18] Y.-M. Lin, K. A. Jenkins, A. Valdes-Garcia, J. P. Small, D. B. Farmer, and Ph. Avouris, Nano Lett. **9**, 422 (2009).

[19] Q. Shao, G. Liu, D. Teweldebrhan, and A. A. Balandin, Appl. Phys. Lett. **92**, 202108 (2008).

[20] P. Blake, E. W. Hill, A. H. Castro Neto, K. S. Novoselov, D. Jiang, R. Yang, T. J. Booth, and A. K. Geim, Appl. Phys. Lett. **91**, 063124 (2007).

[21] Y.-W. Tan, Y. Zhang, H. L. Stormer, and P. Kim, Eur. Phys. J. Spec. Top. **148**, 15 (2007).

[22] K. I. Bolotin, K. J. Sikes, J. Hone, H. L. Stormer, and P. Kim, Phys. Rev. Lett. **101**, 096802 (2008).

[23] T. Ando, J. Phys. Soc. Jpn. **75**, 074716 (2006).

[24] E. H. Hwang and S. Das Sarma, Phys. Rev. B **79**, 165404 (2009).

[25] A. Akturk and N. Goldsman, *Proceedings of the International Conference on Simulation of Semiconductor Processes and Devices (SISPAD)* (IEEE XPLORE, Piscataway, New Jersey, 2008), p. 173.

[26] S. Fratini and F. Guinea, Phys. Rev. B **77**, 195415 (2008).

[27] T. Stauber, N. M. R. Peres, and F. Guinea, Phys. Rev. B **76**, 205423 (2007).

[28] S. V. Morozov, K. S. Novoselov, M. I. Katsnelson, F. Schedin, D. C. Elias, J. A. Jaszczak, and A. K. Geim, Phys. Rev. Lett. **100**, 016602 (2008).

[29] S. Rotkin, V. Perebeinos, A. G. Petrov, and Ph. Avouris, Nano Lett. **9**, 1850 (2009).

[30] M. V. Fischetti, D. A. Neumayer, and E. A. Cartier, J. Appl. Phys. **90**, 4587 (2001).

[31] T. Ohta, A. Bostwick, J. L. McChesney, T. Seyller, K. Horn, and E. Rotenberg, Phys. Rev. Lett. **98**, 206802 (2007).

[32] F. Guinea, Phys. Rev. B **75**, 235433 (2007).

[33] D. Ferry, *Transport in Nanostructure* (Cambridge University Press, Cambridge, England, 2009), Chap. 2.

[34] L. Pietronero, S. Strässler, H. R. Zeller, and M. J. Rice, Phys. Rev. B **22**, 904 (1980).

[35] K. Sugihara, K. Kawamura, and T. Tsuzuku, J. Phys. Soc. Jpn. **47**, 1210 (1979).

[36] Y.-M. Lin and Ph. Avouris, Nano Lett. **8**, 2119 (2008).

[37] A. Deshpande, W. Bao, F. Miao, C. N. Lau, and B. J. LeRoy, Phys. Rev. B **79**, 205411 (2009).

[38] J. Martin, N. Akerman, G. Ulbricht, T. Lohmann, J. H. Smet, K. von Klitzing, and A. Yacoby, Nat. Phys. **4**, 144 (2008).

[39] J. Meyer, A. K. Geim, M. I. Katsnelson, K. S. Novoselov, T. J. Booth, and S. Roth, Nature (London) **446**, 60 (2007).

[40] S. V. Morozov, K. S. Novoselov, M. I. Katsnelson, F. Schedin, L. A. Ponomarenko, D. Jiang, and A. K. Geim, Phys. Rev. Lett. **97**, 016801 (2006).

[41] S. Adam, E. H. Hwang, V. M. Galitski, and S. Das Sarma, Proc. Natl. Acad. Sci. U.S.A. **104**, 18392 (2007).

[42] R. S. Muller and T. Kamins, *Device Electronics for Integrated Circuits*, 2nd ed. (Wiley, New York, 1986), Chap. 1.

[43] S. Datta, *Quantum Transport: Atom to Transistor* (Cambridge University Press, Cambridge, England, 2005), Chap. 7.

[44] A. Das, S. Pisana, B. Chakraborty, S. Piscanec, S. K. Saha, U. V. Waghmare, K. S. Novoselov, H. R. Krishnamurthy, A. K. Geim, A. C. Ferrari, and A. K. Sood, Nat. Nanotechnol. **3**, 210 (2008).